

3D-Printed Autonomous Sensory Composites

Subramanian Sundaram,* Ziwen Jiang, Pitchaya Sitthi-Amorn, David S. Kim, Marc A. Baldo, and Wojciech Matusik

Integrating elements of sensing, embedded computing, and actuation within multimaterial composites, opens a route to nature-inspired autonomous sensory composites.^[1] Insects such as the Golden tortoise beetle (*Charidotella sexpunctata*), shown in **Figure 1A**, consist of a high density of sensorimotor networks that include sensing and actuation mechanisms controlled by local processors in 3D geometries (when the beetle is stressed, it modulates the transparency of its exoskeleton). Sensory composites are manmade analogues of these naturally occurring sensorimotor pathways, and aim to mimic natural functions and improve autonomy in artificial systems. Current fabrication techniques rely on the external assembly of these individual elements that are produced from multiple processes, often limited in topology and density. New additive manufacturing techniques are enabling the rapid creation of functional parts made of advanced materials in complex shapes^[2,3] with multidimensional control.^[4] However, 3D printing is still nascent and building fully integrated systems in unconventional topologies with diverse materials remains a challenging problem. So far, strain sensors,^[5] quantum dot light-emitting diodes,^[6] and passive components have been 3D printed but there is a need for active circuits connected with diverse sensing and response mechanisms. In emerging applications that demand these integrations, such as in robotics and electronics skins,^[7,8] laminates of separately-made high performance sensors^[9] and external processors manufactured using multiple techniques have been used. Much of this progress has been enabled by advances in stretchable materials^[10–12] and ultralight organic electronics.^[13,14] Solution-processed and printable designs have simultaneously emerged from the need for low-cost, large-area manufacturing,^[15–21] in parallel, inspiring our work.

Contemporary approaches, both in the fabrication of individual devices and their subsequent external integration, however, are restricted in structure and by the use of substrates with uniform in-plane properties. Likewise, material choices are constrained; for instance, seamless integration of encapsulated liquids along with thin-film electronics is traditionally hard (see discussion in Supporting Information). We integrate diverse

materials (solids, thin-films, and liquids) and functions into a single seamless autonomous sensory composite by avoiding the use of a premade substrate, and 3D-printing all required materials without any external processing.

We present a monolithic integration of strain sensitive elements with an organic electrochemical transistor (OECT)-based amplifier and an electrochromic element powered at 1.5 V DC fabricated using a low-temperature additive manufacturing approach (additive manufacturing system is shown in **Figure 1B**; integration scheme of the composite is in **Figure 1C** and photograph is shown in **Figure 1D**). There are two challenges in material interface engineering that currently limit the creation of functional 3D composites using a single fabrication method. First, local control of surface energy and texture at material interfaces is essential to assemble multiple materials, specifically for confining solvent inks on solid layers with high fidelity.^[22] Similarly, controlling the droplet deployment order is essential (see the Experimental Section and **Figure S1**, Supporting Information). Second, reducing the operating voltage in active electrical signal processors is strongly tied to achieving defect-free, extremely uniform, thin gate dielectrics in field effect transistors or encapsulating electrolytes in OECTs. We solve this by using a drop-on-demand multimaterial inkjet-based 3D printing platform (see **Figure 1B**) that is capable of printing UV curable materials with a $\approx 35 \mu\text{m}$ lateral resolution^[23] while simultaneously printing solvent-evaporated films, and encapsulated liquids (images of droplets in-flight and printed lines are in **Figure S2**, Supporting Information). Equipped with light-emitting diode (LED) arrays for UV curing, the system can digitally assemble UV curable polymers of varying elastic moduli and surface energies. Droplets of different materials are deployed simultaneously to assemble multiple materials in the same layer, where the resolution is the size of each droplet. When solvent-based inks are printed, a compact ceramic heater on the printhead carriage enables rapid local forced convection heating of the uppermost printed layers. Printed liquids can be confined by sidewalls and also be completely encapsulated inside UV curable matrices. The structure of the final composite to be printed is represented as voxels (volume elements), where the choice of the material for each voxel is made based on the required function. In total, six different materials are printed here (ink compositions are in **Table S1**, Supporting Information); full details of the materials and the printing process are in the Experimental Section and the Supporting Information.

The mechanical matrix of the autonomous sensory composite is made from a basis of two UV curable acrylate polymer materials of varying mechanical stiffness; rigid formulation (elastic modulus $\approx 637.76 \text{ MPa}$) and the elastic material (elastic modulus $\approx 678.5 \text{ kPa}$) span three orders of magnitude in stiffness (**Figure S3**, Supporting Information). The active region

S. Sundaram, Z. Jiang, Dr. P. Sitthi-Amorn, D. S. Kim, Prof. W. Matusik
Computer Science and Artificial Intelligence Lab (CSAIL)
Massachusetts Institute of Technology
Cambridge, MA 02139, USA
E-mail: subras@mit.edu



Prof. M. A. Baldo
Electrical Engineering and Computer Science Department
Massachusetts Institute of Technology
Cambridge, MA 02139, USA

DOI: 10.1002/admt.201600257

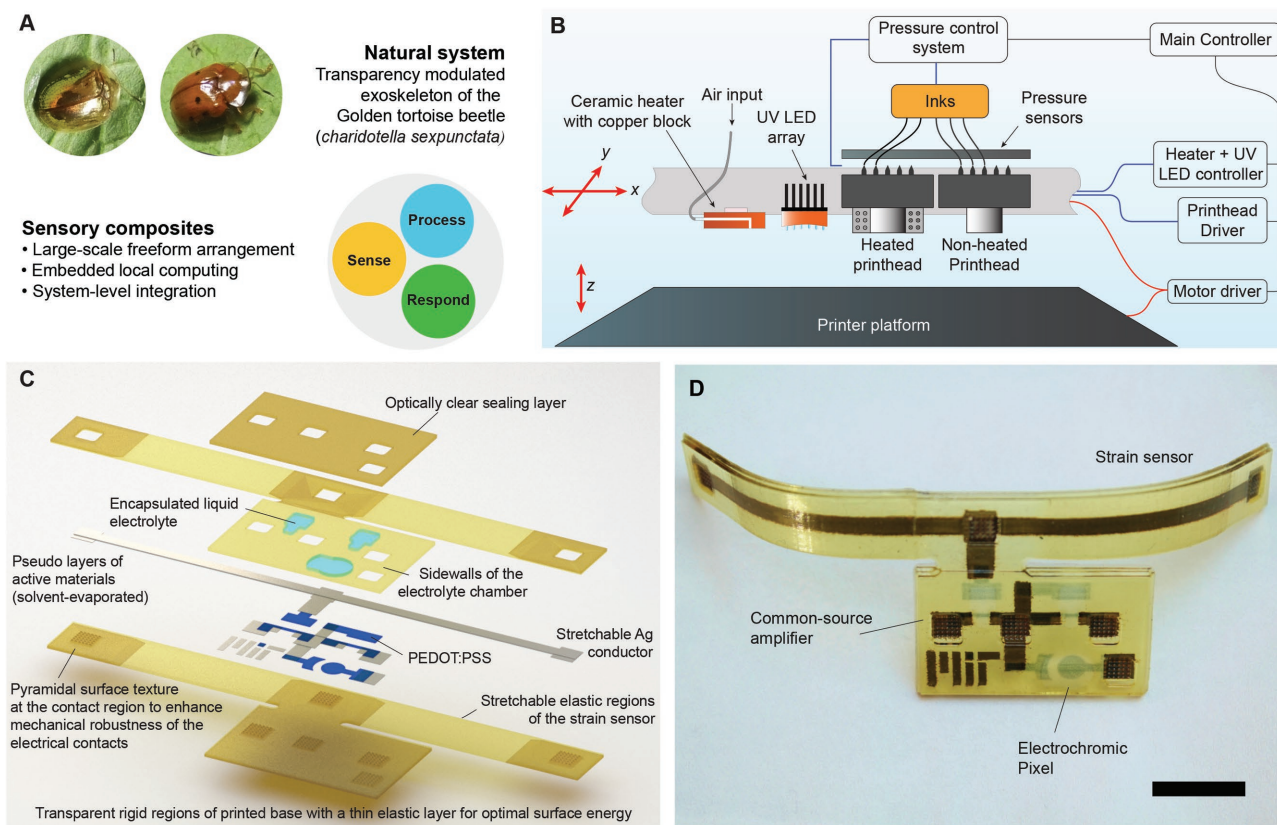


Figure 1. Sensory composites that integrate sensing with locally distributed computing and response mechanisms. a) Illustration of the freeform integration of different functions in efficient systems. In the natural world, the golden tortoise beetle (*Charidotella sexpunctata*) modulates the transparency of its exoskeleton to reveal the underlying red color when it is stressed. (Image credit: S. Leitkam). Inspired by the dense packing of diverse functions, autonomous sensory composites demonstrated here integrate multiple functions in freeform arrangements with access to local signal transduction blocks. b) This is achieved using our drop-on-demand multi-material additive manufacturing platform. The scheme shows the major functional parts of the printer. The two printheads (one of which is heated) can accept a total of up to 10 inks simultaneously. To dispense each droplet, the printhead driver outputs a waveform optimized for the material being dispensed. Printed droplets are UV cured, heated or used in the liquid state. Full details of the printer are in the Supporting Information. c) The composite is grouped into 4 sets of functional layers: a base with spatially varying mechanical stiffness and surface energy, electrical materials, electrolyte, and capping layers. All these materials are printed. The base is formed from droplets of UV curable acrylate polymers. Uppermost layers of the base consist of thin surface energy engineered elastic layers to facilitate proper definition of solvent-based inks. Electrical contact regions of the base are textured with pyramids for mechanically robust contacts. Silver traces are obtained by precipitating silver from a liquid ink by local forced convection heating. The elastic matrix with silver nanoparticles forms a stretchable conductor. Thin PEDOT:PSS layers are obtained by solvent evaporation and are used as the active semiconductor and electrochromic material. The printed conductive and semiconductor materials are capped by UV curable polymers and wells that hold the electrolyte that defines the active transistor geometry. The uppermost optically clear layer seals the electrolyte exposing only the electrical pads. d) Photograph of the fully 3D-printed autonomous sensory composite shows a strain sensor linked to an electrical amplifier that modulates the transparency of the electrochromic pixel (scale bar is 10mm). This is achieved by assembling volume elements (voxels) of multiple materials to transduce signals across multiple domains.

of the strain sensors is fabricated within an elastic matrix, while the electrical contacts, organic amplifier, and the transparency modulator are made rigid. We also explicitly architect the placement of specific materials at the surface and the bulk to control the surface energy and elastic modulus independently. The surface energy plays a crucial role in controlling the shape of the droplet and therefore the quality of features in an inkjet printing process where functional solvent-based inks are printed and evaporated.^[24] The rigid material and the elastic material have surface energies 45.23 and 28.65 mJ m⁻², respectively; surface energy measurements are described in the Experimental Section and Table S2 of the Supporting Information. When solvent inks are printed on a rigid substrate, the high surface energy of the rigid polymer typically forces the liquid

to spread rapidly to a thin film, rendering it unfit for retaining droplets. The elastic polymer with its lower surface energy is able to hold stable patterns in the liquid state until the solvent is evaporated during the forced convective heating passes. Contrast in the surface energy of the two UV curable base materials is used favorably by defining the contact structures with the rigid material to ensure uniform spreading of the ink, while the elastic material is used as a coat where sharp features are printed. Two main solvent-based functional inks we use here are an ink consisting of poly(3,4-ethylenedioxythiophene) doped with poly(styrene sulphonate) (PEDOT:PSS) and an ethanol-based reactive silver ink.^[25] **Figure 2A** shows a photograph of a 1 μ L droplet of the PEDOT:PSS ink on the elastic substrate (contact angle $45.5^\circ \pm 3.1^\circ$).

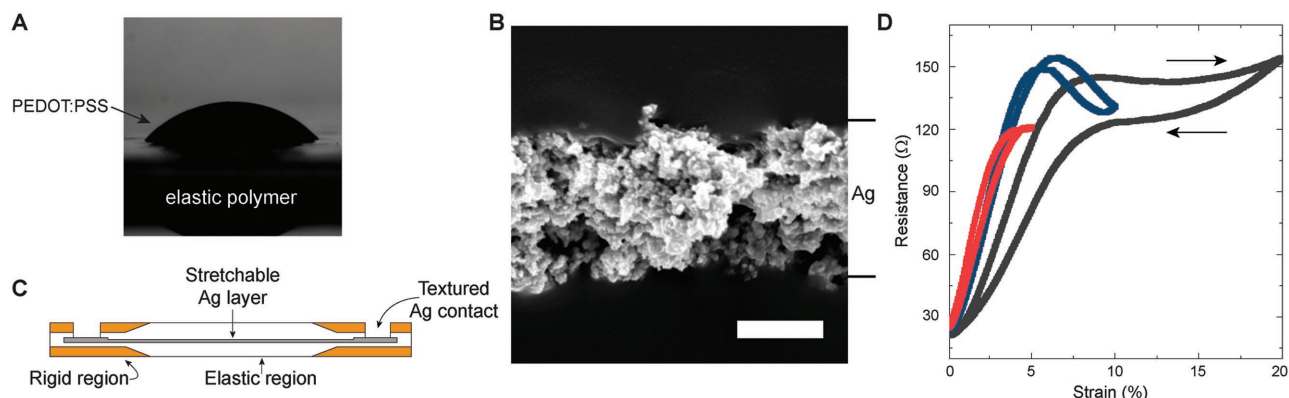


Figure 2. Materials and printed stretchable silver strain sensor. A) Photograph of 1 mL droplet of PEDOT:PSS ink on the elastic substrate (contact angle is $45.5^\circ \pm 3.1^\circ$). When dispensed directly on the rigid polymer surface (surface energy 45.23 mJ m^{-2}), PEDOT:PSS spreads rapidly to form a thin film. The surface energy of the elastic polymer (28.65 mJ m^{-2}) facilitates proper definition of the PEDOT:PSS and silver inks in the liquid state till the solvent can be evaporated. B) Scanning electron microscope image of the cross-section showing the precipitated silver trace between the elastic polymer layers. Scale bar is $5 \mu\text{m}$. C) Schematic of the strain sensor consisting of rigid contact regions, and the elastic polymer regions that enclose the stretchable strain sensitive silver trace. D) Typical resistance of a 20 mm long trace embedded in the elastic polymer matrix, as a function of strain. The sensor is linear up to $\approx 5\%$ elongation, and exhibits low hysteresis. On repeated cycling up to 10% strain, the sensor exhibits sublinear behavior. For higher strain (25%) cycles, the sensor exhibits consistent hysteresis. (Multiple cycles of this measurement for a couple devices are shown in Figure S6, Supporting Information. Characteristics of devices printed across multiple runs and long term cycling tests are shown in Figure S5, Supporting Information. Strain sensors work until mechanical failure of the polymer at high strain as shown in Figure S6C, Supporting Information.)

The active material in the strain sensor is formed by rapid heating of the printed silver ink, facilitating the formation of silver nanoparticles by a reduction reaction. Typically, eight layers of the silver ink (with heater passes every two layers) results in a $10 \mu\text{m}$ thick strain sensitive resistor. The silver traces are sandwiched within the elastic polymer (scanning electron microscope image in Figure 2B) with an outer shell of rigid material at the contacts to form the strain sensor (schematic cross-section is in Figure 2C). The elastic region at the middle of the sensor is 20 mm long, transitioning to a predominantly rigid substrate at the contacts over 1.5 mm (Figure S4, Supporting Information). All our sensors show a linear resistance change as a function of applied strain with no visible hysteresis for small deformations ($\approx 5\%$). Figure 2D shows the resistance as a function of strain when the sensor is cycled uniformly at 10 mm min^{-1} , for varying maximum strains of 5%, 10%, and 20%. The linear gauge factor of the sensor at small strains is 102.94 (see Supporting Information). Our sensors show a small reduction in resistance around 5% elongation. We hypothesize that precipitated nanoparticles are brought closer in the vertical direction as the sensor is stretched horizontally leading to a competing enhanced conductance. On stretching the sensor to 20% strain, the device exhibits hysteresis but shows no remnant offsets over cycles (see Figure S6A,B, Supporting Information). The strain sensors function until mechanical breakage of the polymer (Figure S6C, Supporting Information). In the final system two identical strain sensors are configured into a resistor ladder connected to a dual power supply ($\pm 1.5 \text{ V}$), where one resistor is the active strain sensor while the other permits regulating the transition threshold if needed.

To construct the common source amplifier with a diode-connected load, we use PEDOT:PSS OECTs (cross-sectional schematic shown in Figure 3A). Both the channel and the gate are made with PEDOT:PSS and are bridged by a water-based

electrolyte containing potassium ions. The electrolyte is encapsulated inside a well that defines the channel dimensions. Further, the sidewalls ensure that the silver contacts are not exposed to the halide rich environment, preventing large leakage currents.^[26] The channel of the depletion mode OECT is dedoped by the physical movement of metal ions from the electrolyte when a positive gate voltage is applied. PEDOT:PSS-based OECTs operating up to $\approx 1 \text{ kHz}$ have been demonstrated so far and are capable of amplifying cellular signals.^[27] Typically the speed is limited by the reduction front in the device, which can be improved by utilizing different topologies using carbon paste as the source and drain contact.^[28] Figure 3B shows a scanning electron microscope image of the PEDOT:PSS layer ($\approx 1 \mu\text{m}$ thick sandwiched in the elastic polymer). Transfer characteristics of a transistor with channel width (W) $500 \mu\text{m}$ and length (L) $1500 \mu\text{m}$ are shown in Figure 3D, where the gate-source voltage (V_{gs}) is varied from -0.5 to 1.25 V , with the drain-source voltage (V_{ds}) set to -0.5 V . The on/off current ratio is 9.65×10^3 with a peak transconductance (g_m) of 5.61 mS ($g_m/W = 11.22 \text{ S m}^{-1}$) and an average sub-threshold slope of $152.4 \text{ mV dec}^{-1}$ (Figure S7A, Supporting Information). The current-voltage characteristics are shown in Figure 3E. The switching times of the transistor are typically asymmetric due to the reduction front in the off state, where the off \rightarrow on transition is slower than the on \rightarrow off transient (Figure S7C, Supporting Information). Figure S7B of the Supporting Information shows the transfer curves of six transistors printed in multiple runs. The transistor is connected to an active load to form the amplifier (as shown in Figure 3C), where the gain is proportional to the load resistance (input-output characteristics shown in Figure S7E, Supporting Information). Here, the channel length of the diode connected transistor is $2L$ ($3000 \mu\text{m}$). As the mismatch between the channel lengths of the load and the active transistor is increased, the output swing reaches closer to the ideal rail-to-rail switching characteristics,

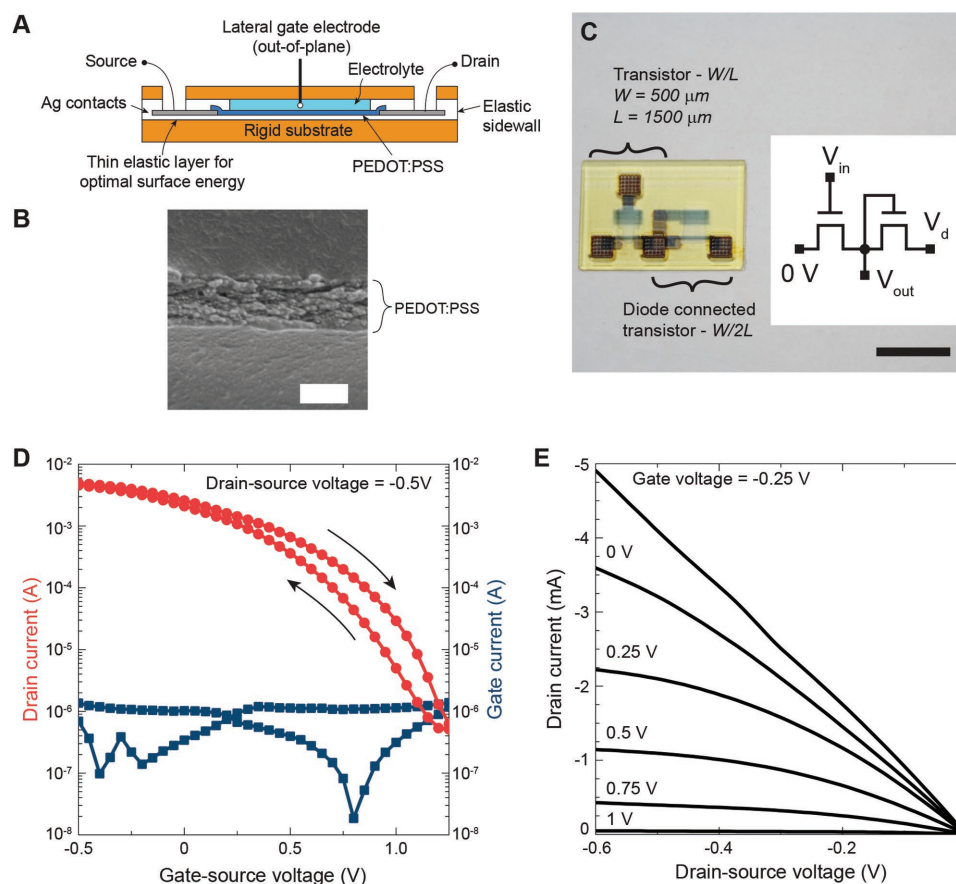


Figure 3. Printed depletion mode p-type PEDOT:PSS transistors. a) A cross-sectional schematic of the transistor is shown. b) Scanning electron microscope image of PEDOT:PSS layer between elastic polymer layers. Scale bar is 1 μm . c) Photograph of a transistor amplifier with a diode connected load. Transistor width, $W = 500 \mu\text{m}$ and length, $L = 1500 \mu\text{m}$. The diode connected transistor has a length $2L = 3000 \mu\text{m}$. Scale bar is 10 mm. (Performance characteristics of diode connected loads, and the input-output characteristics of the amplifier are in Figure S7d and Figure S7e respectively.) d) Drain current and gate current of a transistor as a function of the gate-source voltage. Transistor has width, $W = 500 \mu\text{m}$ and length, $L = 1500 \mu\text{m}$. e) Transistor I - V curves showing drain current as a function of drain voltage, for gate voltage between -0.25 V and 1 V , in steps of 0.25 V . (Plots of the transconductance and sub-threshold swing, response time and characteristics of multiple devices printed in separate runs are in Figure S7.)

while simultaneously shifting the maximum gain bias-voltage higher.

The strain sensor (R_2)-based resistor ladder, common source amplifier, and the transparency modulator are connected together as shown in the circuit in Figure 4A. Transistors M_1 and M_2 are made identical in channel geometry to achieve maximum gain at $\approx 0 \text{ V}$ (Figure 4B shows the input-output curve and the gain), which is the default voltage at the intermediate node in the resistor ladder. In this default state, the voltage across the pixel is $\approx 0.7 \text{ V}$, leaving it in a dark state. As R_2 is stretched, the voltage input to the amplifier is positive, leading to a drop in the voltage across the electrochromic pixel. We use the optical contrast in the optical absorption spectrum between oxidized (transparent) and reduced states of the PEDOT:PSS film^[29] to make switchable transparency elements shown in the schematic in Figure 4C. When the voltage across the pixel is varied, the transmission through the device changes (Figure 4D shows photographs; Figure 4E contains transmission spectra through the pixel). Figure 4F shows two frames from a video of the fully integrated system, highlighting the color change as the regulator (R_1) and the sensor (R_2) are

deformed. Raw real-time video of the system is included in Movie S1 (Supporting Information). Such composites can be further enhanced by the seamless integration of hydraulics (see Figure S8 and description in Supporting Information). Merging hydraulics and electronics within a single composite containing soft materials allows control of both the shape and color as shown. Further, microfluidics-based biosensors often rely on having active electronic devices inside microfluidic channels. Overall, the biggest challenge is in integrating power sources within the composite. Reducing the need for external power sources (and wires) would be an important direction toward self-sufficiency in these autonomous sensory composites.

The monolithic integration of sensing, processing and response mechanisms shown here allows transducing signals across mechanical, electrical, and optical domains using low-power organic processors and sensors that can be powered by 1.5 V . Controlling multidomain properties with uniform resolution and without any external processing should enable advances in biologically inspired autonomous multifunctional systems with increased local signal processing efficiencies and

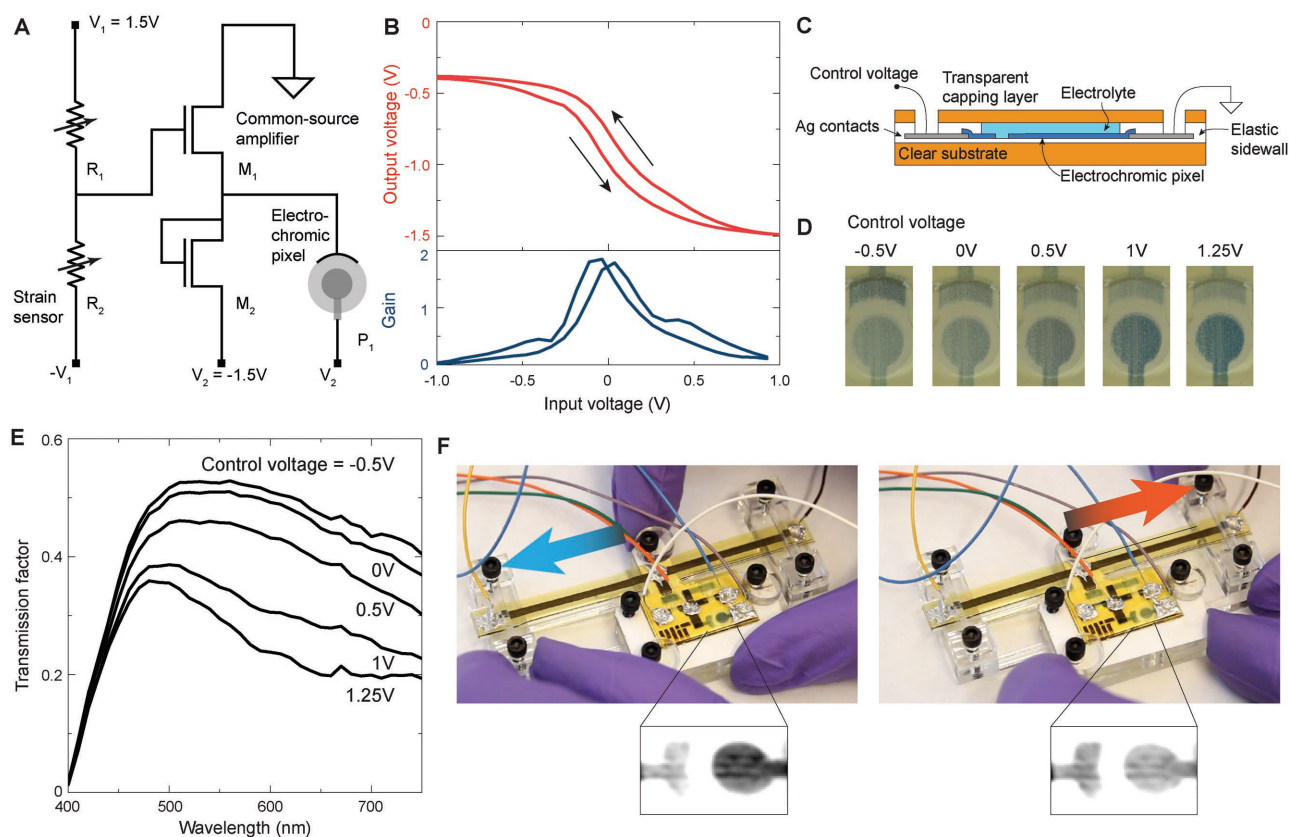


Figure 4. Printed integrated organic sensing system with electrochromic output. A) Equivalent circuit diagram of the strain sensor ladder, the common source amplifier with a diode-connected transistor load, and the electrochromic pixel. B) Output voltage and gain as a function of the voltage at the input of the transistor M_1 in (A). Transistors M_1 and M_2 are matched to achieve maximum gain at 0 V. Transistor width, $W = 500 \mu\text{m}$ and length, $L = 1500 \mu\text{m}$. C) Schematic cross-section of the electrochromic pixel. D) The transmitted color through the sealed printed pixel placed above a white paper in natural light. The circular pixel is dedoped (reduced) as the control voltage is increased. E) Transmission spectrum through the printed pixel normalized with respect to direct transmission using a 2 mm aperture. F) Output at the electrochromic pixel when the left (R_1) and right (R_2) strain sensors are extended. At rest, the pixel is in the dark reduced state due to the default voltage ($\approx 0.7 \text{ V}$) across the pixel. Transparency is increased when R_2 is extended, and the voltage across the pixel drops closer to 0 V. Contrast enhanced red channel information from the frames are shown in the monochrome close up. Movie S1 of the Supporting Information shows a real-time video of the system.

levels of self-sufficiency currently only seen in nature. With room for miniaturization and a prospect for using biocompatible structural matrices, this approach could lead to compact autonomous systems that interface with or support natural biological systems.

Experimental Section

The full details of the printer and the printing process are described in the Supporting Information.

Ink Preparation: Inks used in this work were prepared in the wet lab from constituent materials bought from different commercial vendors. Each ink was optimized for desired functional properties and subsequently had its rheological properties^[30] tuned to make it suitable for inkjet printing. The UV curable inks were formulated based on the prior work^[23] and prepared by mixing all individual constituents together with a magnetic bead stirrer overnight. Silver ink was prepared based on an ethanol-based formulation using an approach described in a patent.^[25] A neutral PEDOT:PSS based formulation (Clevios P Jet 700N, Heraeus, Leverkusen, Germany) was mixed with 5% dimethyl sulfoxide (A13280 Dimethyl sulfoxide, 99+%, Alfa Aesar, USA) to prepare the PEDOT:PSS ink used here. The liquid electrolyte used for the gate was a

0.1 M solution of potassium chloride in deionized (DI) water, mixed with glycerol. Table S1 of the Supporting Information shows the components of each ink and their ratios.

Waveform Optimization: Before each ink was printed, the waveform input to the piezoelectric actuator in the printhead channel was optimized using a stroboscopic illumination technique, allowing one to probe the evolution of the droplet at the nozzle. This was performed using a drop-in-flight analysis system from jetXpert. At this point, the printhead used was mounted to a stationary stage. The temperature of the printhead, pressure of the ink in the channel, and firing frequency were set to desired values as the voltage waveform was optimized for each ink. Further, once the droplet quality was optimized to produce single droplets for each pulse with no satellite drops, the velocity and the droplet volume were matched for different inks. The optimized waveform for each ink was saved and used as an input in the printer software, matching the print conditions.

Characterization and Electrical Testing: Wires were attached to the open textured contacts with low temperature curing conductive silver epoxy (MG Chemicals 8331 Two-part silver conductive epoxy adhesive, Amazon, USA). The attached wires were left undisturbed overnight for the epoxy to cure at room temperature. Typically, devices were tested 2 d after printing for uniformity. All devices were printed and stored in ambient conditions exposed to open air. It was observed that the encapsulated solution does not evaporate at least until one to two weeks after print.

Mechanical stress–strain tests for supporting UV curable polymer materials were performed with Instron 5944 (Instron, Norwood, MA, USA), a single column table top mechanical testing system. Surface profile measurements of the textured contact were obtained using a GelSight Benchtop Scanner (GelSight Inc., Waltham, MA, USA). Printed strain sensor characterization was performed by using the Instron 5944 to strain cycle the sample, while the resistance was measured using a Keithley 2611B sourcemeter with 100 mV applied across the sample. Steady state transistor characterization and amplifier measurements were performed using an Agilent 4155C Semiconductor Parameter Analyzer. To measure the transient characteristics of the transistors, an Agilent 33250A signal generator was used to generate the gate voltage control pulse (−0.25 V low voltage, 1 V high voltage, 50% duty cycle, 0.1 Hz frequency, for measurement in Figure S7C, Supporting Information), while the drain current was measured using the Keithley 2611B sourcemeter. Transmission spectra were measured using a spectrophotometer (X-Rite Color i5 Benchtop Spectrophotometer, X-Rite Inc., Grand Rapids, MI, USA) using a Keithley 2611B as the control voltage power source.

Integrated Composite Image and Video: The functional sensory composite was recorded with a Canon EOS 60D, and the unedited version is shown in Movie S1 of the Supporting Information. The zoomed in pixel shows the stabilized close-up of the electrochromic pixel in original color. The pixel intensity meter shows the value of the average intensity in the active area of the pixel for each frame and is calculated using MATLAB. For the zoomed-in monochrome images of the pixel regions shown in Figure 4F, the red channel of the image is contrast enhanced consistently in all parts.

Contact Angle Measurements and Surface Energy Calculations: The surface energy of samples was calculated by using the van Oss–Good–Chaudhury approach,^[31,32] with measurements of contact angles made by three probe liquids on the smooth side of samples printed on a glass slide. The three reference probe fluids used here were DI water, ethylene glycol, and diiodomethane. The total surface energy of the solid material, γ^{tot} , is a sum of the Lifshitz–van der Waals (apolar) component, γ^{LW} , and the polar Lewis acid–base component, γ^{AB} . The polar component was computed from the individual Lewis acid and Lewis base components as $\gamma^{\text{AB}} = 2\sqrt{\gamma^+ \gamma^-}$. From the acid–base theory of contact angles, the complete version of the Young equation is written as $(1 + \cos \theta) \gamma^{\text{tot}} = 2(\sqrt{\gamma_s^{\text{LW}} \gamma_l^{\text{LW}}} + \sqrt{\gamma_s^+ \gamma_l^-} + \sqrt{\gamma_s^- \gamma_l^+})$, where the subscripts S and L denote the solid surface and the specific liquid and θ is the contact angle. The values of the measured contact angles, γ^{tot} , γ^{LW} , γ^+ , and γ^- of the reference fluids (known) and the calculated values of surface energies for the two polymers are shown in Table S2 of the Supporting Information. The contact angles were measured using the VCA-2000 Video Contact Angle System Goniometer (AST Products Inc., Billerica, MA, USA).

Supporting Information

Supporting Information is available from the Wiley Online Library or from the author.

Acknowledgements

This work was supported by the DARPA SIMPLEX program through SPAWAR. The views expressed are those of the authors and do not reflect the official policy or position of the DoD or the US Government. MIT has filed a provisional patent application (No. 62/277764) based on this work. The authors would like to thank Daniel Piedra for help in transistor characterization and Wenshou Wang for developing UV curable inks described in ref. [23] and help with obtaining scanning electron microscope images.

Received: November 8, 2016

Revised: December 2, 2016

Published online: January 4, 2017

- [1] M. McEvoy, N. Correll, *Science* **2015**, *347*, 1261689.
- [2] J. Tumbleston, D. Shirvanyants, N. Ermoshkin, R. Januszewicz, A. Johnson, D. Kelly, K. Chen, R. Pinschmidt, J. Rolland, A. Ermoshkin, E. Samulski, J. DeSimone, *Science* **2015**, *347*, 1349.
- [3] Z. Eckel, C. Zhou, J. Martin, A. Jacobsen, W. Carter, T. Schaedler, *Science* **2016**, *351*, 58.
- [4] D. Kokkinis, M. Schaffner, A. Studart, *Nat. Commun.* **2015**, *6*, 8643.
- [5] J. Muth, D. Vogt, R. Truby, Y. Mengüç, D. Kolesky, R. Wood, J. Lewis, *Adv. Mater.* **2014**, *26*, 6307.
- [6] Y. Kong, I. Tamargo, H. Kim, B. Johnson, M. Gupta, T. Koh, H. Chin, D. Steingart, B. Rand, M. McAlpine, *Nano Lett.* **2014**, *14*, 7017.
- [7] B. Tee, A. Chortos, A. Berndt, A. Nguyen, A. Tom, A. McGuire, Z. Lin, K. Tien, W. Bae, H. Wang, P. Mei, H. Chou, B. Cui, K. Deisseroth, T. Ng, Z. Bao, *Science* **2015**, *350*, 313.
- [8] H. Chou, A. Nguyen, A. Chortos, J. To, C. Lu, J. Mei, T. Kurosawa, W. Bae, J. Tok, Z. Bao, *Nat. Commun.* **2015**, *6*, 8011.
- [9] S. Mannsfeld, B. Tee, R. Stoltenberg, C. Chen, S. Barman, B. Muir, A. Sokolov, C. Reese, Z. Bao, *Nat. Mater.* **2010**, *9*, 859.
- [10] J. Rogers, T. Someya, Y. Huang, *Science* **2010**, *327*, 1603.
- [11] D. Kim, N. Lu, R. Ma, Y. Kim, R. Kim, S. Wang, J. Wu, S. Won, H. Tao, A. Islam, K. Yu, T. Kim, R. Chowdhury, M. Ying, L. Xu, M. Li, H. Chung, H. Keum, M. McCormick, P. Liu, Y. Zhang, F. Omenetto, Y. Huang, T. Coleman, J. Rogers, *Science* **2011**, *333*, 838.
- [12] C. Larson, B. Peele, S. Li, S. Robinson, M. Totaro, L. Beccai, B. Mazzolai, R. Shepherd, *Science* **2016**, *351*, 1071.
- [13] T. Sekitani, U. Zschieschang, H. Klauk, T. Someya, *Nat. Mater.* **2010**, *9*, 1015.
- [14] M. Kaltenbrunner, T. Sekitani, J. Reeder, T. Yokota, K. Kuribara, T. Tokuhara, M. Drack, R. Schwödiauer, I. Graz, S. Bauer-Gogonea, S. Bauer, T. Someya, *Nature* **2013**, *499*, 458.
- [15] B. Crone, A. Dodabalapur, Y. Lin, R. Filas, Z. Bao, A. LaDuca, R. Sarpeshkar, H. Katz, W. Li, *Nature* **2000**, *403*, 521.
- [16] H. Klauk, U. Zschieschang, J. Pfau, M. Halik, *Nature* **2007**, *445*, 745.
- [17] J. Cho, J. Lee, Y. Xia, B. Kim, Y. He, M. Renn, T. Lodge, C. Daniel Frisbie, *Nat. Mater.* **2008**, *7*, 900.
- [18] H. Sirringhaus, T. Kawase, R. Friend, T. Shimoda, M. Inbasekaran, W. Wu, E. Woo, *Science* **2000**, *290*, 2123.
- [19] H. Yan, Z. Chen, Y. Zheng, C. Newman, J. Quinn, F. Dötz, M. Kastler, A. Facchetti, *Nature* **2009**, *457*, 679.
- [20] M. Berggren, D. Nilsson, N. Robinson, *Nat. Mater.* **2007**, *6*, 3.
- [21] J. Choi, H. Wang, S. Oh, T. Paik, P. Sung, J. Sung, X. Ye, T. Zhao, B. Diroll, C. Murray, C. Kagan, *Science* **2016**, *352*, 205.
- [22] A. Mahajan, W. Hyun, S. Walker, G. Rojas, J. Choi, J. Lewis, L. Francis, C. Frisbie, *Adv. Electron. Mater.* **2015**, *1*, 9.
- [23] P. Sitthi-Amorn, J. Ramos, Y. Wang, J. Kwan, J. Lan, W. Wang, W. Matusik, *ACM Trans. Graph.* **2015**, *34*, 129.
- [24] D. Soltman, V. Subramanian, *Langmuir* **2008**, *24*, 2224.
- [25] S. B. Walker, J. A. Lewis, US Patent No. 2015/0004325 A1, **2015**.
- [26] G. Tarabella, C. Santato, S. Yang, S. Iannotta, G. Malliaras, F. Cicoira, *Appl. Phys. Lett.* **2010**, *97*, 123304.
- [27] D. Khodagholy, J. Rivnay, M. Sessolo, M. Gurfinkel, P. Leleux, L. Jimison, E. Stavrinidou, T. Herve, S. Sanaur, R. Owens, G. Malliaras, *Nat. Commun.* **2013**, *4*, 2133.
- [28] P. Andersson Ersman, D. Nilsson, J. Kawahara, G. Gustafsson, M. Berggren, *Org. Electron.* **2013**, *14*, 1276.
- [29] P. Andersson, D. Nilsson, P. Svensson, M. Chen, A. Malmström, T. Remonen, T. Kugler, M. Berggren, *Adv. Mater.* **2002**, *14*, 1460.
- [30] B. Derby, *Annu. Rev. Mater. Res.* **2010**, *40*, 395.
- [31] C. Van Oss, R. Good, M. Chaudhury, *Langmuir* **1988**, *4*, 884.
- [32] G. Azimi, Y. Cui, A. Sabanska, K. Varanasi, *Appl. Surf. Sci.* **2014**, *313*, 591.